Chemical Science

ROYAL SOCIETY OF CHEMISTRY

EDGE ARTICLE

View Article Online
View Journal | View Issue

Cite this: *Chem. Sci.*, 2024, **15**, 5539

All publication charges for this article have been paid for by the Royal Society of Chemistry

Received 18th January 2024
Accepted 6th March 2024

DOI: 10.1039/d4sc00423j

rsc.li/chemical-science

Amplifying dual-visible-light photoswitching in aqueous media *via* confinement promoted triplet–triplet energy transfer†

Wenhui Wang,‡[a] Weixin Yang,‡[a] Zhiwei Zhang,‡[a] Jinghong Dai,[a] Yisheng Xu[b] and Junji Zhang *[a]

Achieving visible-light photochromism is a long-term goal of chemists keen to exploit the opportunities of molecular photoswitches in multi-disciplinary research studies. Triplet-sensitization offers a flexible approach to building diverse visible-light photoswitches using existing photochromic scaffolds, circumventing the need for sophisticated molecular design and synthesis. Unfortunately, distance-dependence and environment-sensitivity of triplet-excited species remain as key challenges that severely impair sensitization efficiency and limit their practical availability. We present herein a nature-inspired nanoconfinement strategy in which a triplet-sensitized visible-light photoswitch/sensitizer system is assembled into nanoconfined micelles ($d \sim 40$ nm). A *ca.* 10-fold efficiency increase of triplet–triplet energy transfer for photochromism as well as an amplified fluorescence on/off contrast upon bi-directional visible-light excitation (470/560 nm) was achieved in full aqueous media. By virtue of this, the hybrid photoswitchable system is successfully applied for both flash information encryption and multiple dynamic cell imaging assays, further proving its versatility in materials and life science.

Introduction

Molecular photoswitches attract growing interest as a means to control biosystems non-invasively and with high spatiotemporal resolution.[1–3] Most commonly, such systems require operation with high-energy UV light, which is deleterious to cells and unable to penetrate effectively through biological tissue. Thus, the operation of photoswitches with biocompatible visible-light is an attractive goal.[3–7] Substantial efforts have been directed towards the development of photoswitchable compounds that are responsive in the region of 400–700 nm, either through elaborate molecular design/synthesis (*e.g.*, π-system elongation,[8,9] electronic push–pull structures,[10,11] newly discovered photochromic molecules[12–14]) or through alternative photochemical pathways (*e.g.*, triplet-sensitization,[15–26] triplet–triplet annihilation,[27] multi-photon excitation[28,29]). We previously introduced a facile strategy to achieve highly efficient visible-light photochromism *via* triplet sensitization with narrow ΔE_{ST} sensitizers.[19,20] Triplet-sensitization relies on access to the intrinsic low-lying excited triplet state of an auxiliary photosensitizer which subsequently donates energy to the chromophore to trigger the photoswitching reaction pathway. In addition to the intensive visible-light absorption and effective intersystem crossing, the narrow ΔE_{ST} sensitizers guarantee an on-demand screening of sensitizer–photoswitch pairs by easily fitting their triplet-energy levels, which is compatible with existing high-efficiency photoswitches. This strategy thus circumvents the requirement for elaborate design, synthesis and optimization of novel photoswitches, and offers a general approach for the versatility of visible-light switch fabrication. Furthermore, the indirect low-energy excitation of an auxiliary sensitizer protects the photoswitch from over-exposure, conferring additional photostability which renders the system more robust in practical applications. Whilst the progress is promising, features of environment-sensitivity and distance-dependence for triplet-sensitization still remain as the "Achilles heel" towards real applications, especially in biological scenarios. Firstly, the excited triplet states of both photosensitizer/photoswitch would be quenched or influenced by molecular oxygen (biological systems cannot readily be de-aerated) and solvent polarity (most biological systems are in polar aqueous media). Secondly, the Dexter-type electron exchange mechanism just allows a rather short diffusion distance (<1 nm) for efficient energy transfer. In a word, enhancing the energy/electron migration efficiency and suppressing other competing de-activation processes during

[a]*Key Laboratory for Advanced Materials and Joint International Research Laboratory of Precision Chemistry and Molecular Engineering, Feringa Nobel Prize Scientist Joint Research Center, School of Chemistry and Molecular Engineering, East China University of Science & Technology, 130 Meilong Road, Shanghai, 200237, China. E-mail: zhangjunji@ecust.edu.cn*

[b]*State Key Laboratory of Chemical Engineering, East China University of Science & Technology, 130 Meilong Road, Shanghai, 200237, China*

† Electronic supplementary information (ESI) available. See DOI: https://doi.org/10.1039/d4sc00423j

‡ These authors contributed equally: Wenhui Wang, Weixin Yang, Zhiwei Zhang.

molecular collision/diffusion is the essence to realize multi-functional applications of visible-light photoswitches from current molecular model systems.

The phenomenon of self-assembly and supramolecular confinement is harnessed by nature to carry out unique multi-component photo/biochemical transformations with high efficiency.[30–35] In contrast to diffusional processes operating in bulk solution, confined environments significantly reduce diffusional distances and enrich local concentrations of the reactive species.[36] This may significantly alter both the thermodynamic and kinetic parameters of chemical reactions, and also modulate the efficiency of energy/electron transfer processes.[34,35,37] For example, the ordered self-assembly of supercomplex photosystem I/II and peripheral antennas in biomembranes well controls the alignment of these functional units and ensures the highly effective energy/electron transfer that completes the photosynthetic light–matter conversion (Fig. 1a).[38–40] Moreover, molecular confinement may also shield the reactive species from external quenchers (*e.g.*, O_2, water) to stabilize the reactive intermediates.[41–45] Inspired by the delicacy of natural bio-systems, much attention has been devoted toward the design of biomimetic nano-confined photoswitchable systems towards the goal of achieving the hitherto elusive applications of isolated molecular photoswitches.[21,46–49] The benefits of molecular confinement of photoswitches include protecting their well-controlled switching behaviors against steric hindrance[50] and aggregation,[51] manipulating the equilibrium of the photostationary state,[15] as well as stabilizing the excited state intermediates to achieve enhanced fatigue resistance of the photosystems.[52] In this light, we opine that the archetypal essence of bio-confinement would offer a synergistic method to address simultaneously the challenges of triplet-sensitized photochromism and boost the multi-scenario applications of visible-light photoswitches.

Herein, we present the design of a "three-in-one" visible-light responsive system based on the simple integration of a diarylethene photoswitch and a triplet-sensitizer within a micelle (Diarylethene-Sensitizer@Micelle, **DS@M**, Fig. 1b). The advantages conferred by this molecular confinement approach are: (1) local concentration enrichment significantly decreases the diffusional distance between the sensitizer and the open diarylethene isomer, thus attenuating the distance-dependence and promoting the triplet energy transfer process; (2) the shielding effect of the micelle protects the excited triplet states from being influenced by oxygen/solvent polarity, thus eliminating the environment-sensitivity and some de-activation pathways. Moreover, spectral overlap between the fluorescence of the sensitizer (λ_{em} = 540 nm) and absorption of closed diarylethene (λ_{abs} = 560 nm; fluorescence quencher) leads to an additional FRET process, which is also amplified due to the cooperative spatial confinement (shortened ET distance and high yield of the closed diarylethene quencher) and further enriches its functions and availability for application diversity. As a result, *ca.* 10-fold enhancement of visible-light photochromism (λ_{ex} = 475/560 nm) together with a high-rate and high-contrast ($k_{ET} = 6.86 \times 10^{13}$ s^{-1}, ET = 94.5%) on/off fluorescence modulation in a full aqueous phase was observed. The micelles were fully soluble in aqueous solution without the need to introduce further design complexity, and dispersible in hydrogel matrices to afford a flash (<1 s) photo-reversible information encryption/decryption system. Finally, the biocompatible visible-light photoswitching and corresponding high-contrast "photo-blinking" afforded within the micelle nanoconfinement were exploited for multi-modal fluorescence confocal/lifetime imaging microscopy and super-resolution STORM (stochastic optical reconstruction microscopy) imaging in HeLa cells, achieving an image resolution of 60 nm.

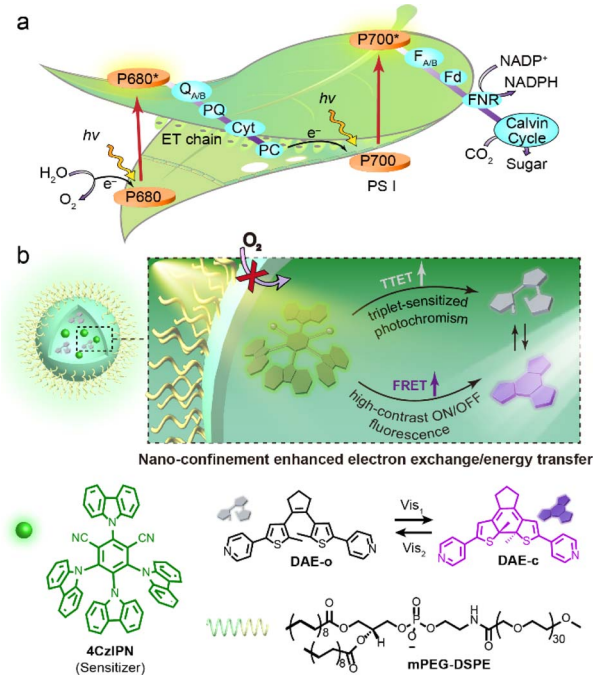

Fig. 1 (a) The efficient energy/electron transfer process that occurs during the photosynthetic light–matter conversion. (b) Top: schematic representation of nano-confinement enhanced electron exchange/energy transfer. Bottom: structures of 4CzIPN (sensitizer), DAE (photoswitch) and mPEG-DSPE (amphiphile).

Results and discussion

Preparation and characterization of a nanoconfined triplet-sensitized visible-light photochromic system

A photoswitch/photosensitizer pair, diarylethene (**DAE**) and **4CzIPN** (a classic narrow ΔE_{ST} sensitizer), was selected according to the matched triplet energy levels of the photoswitch and photosensitizer components (**DAE-o**, S_1 = 4.19 eV, T_1 = 2.40 eV; **4CzIPN**, S_1 = 2.55 eV, T_1 = 2.43 eV; Table S2; see the ESI† for details). **DAE-o**/**4CzIPN** was then incorporated within the **mPEG-DSPE** micelle shell to form the photochromic nano-confinement system **DS@M** (Fig. 1b). The average co-encapsulation ratio was calculated as **DAE-o : 4CzIPN** = 1 : 1 according to the respective absorption spectra. Photochromic micelles were prepared by a kinetically controlled flash nano-precipitation (FNP) method in which the organic phase (with **DAE-o**/**4CzIPN** dissolved) was rapidly mixed with the aqueous

phase (with **mPEG-DSPE** dissolved) in a short time (~milliseconds) to give a homogeneous colloidal solution of uniformly distributed, small-sized micelle nanoparticles (Fig. S1, see the ESI† for details).[53] Dynamic light scattering (DLS) indicated that the synthesized micelle possesses an average hydrodynamic diameter of *ca.* 40 nm with a poly-dispersion index (PDI) of 0.1 (Fig. S3†), which was further confirmed by transmission electron microscopy (TEM; Fig. S4†). The stability of the micelle solution was examined after storage at room temperature in the dark for over 4 weeks. No obvious particle size and PDI changes were observed, revealing the high durability and aqueous solubility of the nanoconfinement system. Control systems of micelle nanoconfinements containing either only the photoswitch **DAE-o** (**D@M**) or only the sensitizer **4CzIPN** (**S@M**) were synthesized using the same method.

The triplet-sensitized visible-light photochromism of **DS@M** was investigated in PBS buffer (2.5×10^{-5} M, 2 mL) upon alternate irradiation with 475/560 nm light. Illumination at 475 nm (10 mW cm^{-2}, 30 s) triggered the fast appearance of a new absorption band around 560 nm (Fig. 2b and S5†), indicating the generation of the closed isomer **DAE-c** (the characteristic absorption band is identical to that formed under direct UV-induced cyclization in both solution and micelle, Fig. S6†). The photostationary state (PSS) displayed a decent thermal stability for more than 1 week at room temperature in the dark (Fig. S7†), conforming to the P-type photochromic behaviour of diarylethenes.[2] Upon illumination with 560 nm light (30 mW cm^{-2}, 2 min) the spectrum of the original **DAE-o** was completely regenerated, demonstrating a full cycle of photocyclization/cycloreversion (Fig. 2b). No photochromic behavior was observed upon 475 nm irradiation of micelles containing **DAE-o** but lacking the presence of the photosensitizer (**D@M**) (Fig. S6†), which eliminates the possibility that the photochromic behavior of **DS@M** results from the direct excitation of **DAE-o**. Indeed, these results confirm that the visible-light photochromism of **DS@M** stems from the intermolecular triplet–triplet energy transfer (TTET) from the **4CzIPN** sensitizer to the **DAE-o** photoswitch (Fig. 2a).

Enhanced triplet–triplet energy transfer in DS@M

The effective visible-light photochromism of the **DS@M** system prompted us to further study the nanoconfinement effect that promotes the triplet-sensitization process. A control sample was constructed by preparing a mixed solution of freely diffusing **DAE-o** and **4CzIPN** (1 : 1) without **mPEG-DSPE** micellar confinement (2.5×10^{-5} M in 2 mL tetrahydrofuran, THF). As shown in Fig. 2c, the **DAE-o**/**4CzIPN** mixed solution exhibited a significantly reduced yield and rate of visible-light photochromism (ΔA@560 nm = 0.015, 10 mW cm^{-2}@475 nm), corresponding to a 9-fold decrease in quantum yield ($\Phi_{o-c} = 0.89\%$) compared to the **DS@M** system (ΔA@560 nm = 0.16, 10 mW cm^{-2}@475 nm; $\Phi_{o-c} = 7.75\%$). Considering the charge-transfer feature of the triplet-sensitizer (twisted donor–acceptor structure of **4CzIPN**),[20,54] the possible solvent polarity effect (consequently alters excited energy levels) on the visible-light photochromism was also checked (Fig. 2g and S12†). As expected, incomparable photochromic efficiency was exhibited in all de-aerated solvents (from the low-polarity toluene to the high-polarity DMSO) towards **DS@M** in PBS buffer (see the following section for details). The above results indicate the essential role of molecular diffusion in the triplet-sensitized visible-light photochromic system.

To more deeply investigate the effect of nanoconfinement on the visible-light photochromism, we turned to transient absorption spectroscopy to obtain further evidence for the enhanced triplet energy-transfer process between **DAE-o** and **4CzIPN** in **DS@M** by monitoring the decay of the transient absorbance intensity at 477 nm (**4CzIPN**) upon nanosecond-pulsed laser excitation. The transient absorption decays at 477 nm under both aerated and de-aerated conditions were measured (Fig. S8 and S9†). A faster decay ($\tau = 0.504$ μs) was detected in aerated THF as compared to that in de-aerated THF ($\tau = 1.311$ μs), and thus the transient absorption band at 477 nm was attributed to the triplet excited state of **4CzIPN**. After argon bubbling, we first checked the transient absorption decay at 477 nm in **DAE-o**/**4CzIPN** mixed solution without micellar confinement of the two species. As expected, a moderate decrease of the triplet excited lifetime ($\tau = 0.623$ μs) was observed (*ca.* 47%), indicating the existence of intermolecular TTET process (Fig. 2d, top). In contrast, when **4CzIPN** was co-encapsulated with **DAE-o** in **DS@M**, a significantly reduced lifetime ($\tau < 0.1$ μs, corresponding to an almost completely quenched triplet excited state; Fig. 2d, bottom) was observed, compared with that of **4CzIPN** alone in the control **S@M** micelle ($\tau = 1.250$ μs). These results demonstrate the superior efficiency of the TTET process within the nanoconfined micelle system.

On account of the narrow gap between the S_1 and T_1 levels of **4CzIPN**, both delayed fluorescence and phosphorescence measurements can be utilized to characterize the excited triplet state of the **4CzIPN** sensitizer. Accordingly, the TTET process was also validated by examining the luminescence properties of both micelle-confined and mixed diffusional bulk solutions of **4CzIPN** and **DAE-o**. The lifetime of the delayed fluorescence of **4CzIPN** fell sharply from $\tau = 1.83$ μs (**4CzIPN** alone in **S@M**) to $\tau = 0.12$ μs (**DAE-o**/**4CzIPN** pair in **DS@M**; Fig. 2e). In a bulk solution of **DAE**/**4CzIPN**, an attenuated decrease of the **4CzIPN** delayed fluorescence lifetime was obtained ($\tau = 3.13$ μs to 2.59 μs; Fig. 2e). Similar results were acquired in phosphorescence lifetime measurements at 77 K. The lifetime varies from $\tau = 1368$ μs to 780 μs in micelles, while from $\tau = 1757$ μs to 1679 μs in the mixed solution (Fig. S10†). The above results demonstrate again the remarkably enhanced visible-light photochromism within the **DS@M** nanoconfinement by shortening the spatial distance between the photoswitch and sensitizer molecules, thus benefitting the Dexter-type intermolecular TTET process.

The environment-shielding effect of DS@M

The vulnerability of triplet-sensitization processes towards triplet quenching agents (*e.g.*, molecular oxygen) imposes a severe limitation on their applications, especially under physiological conditions. Indeed, the oxygen-quenching effect

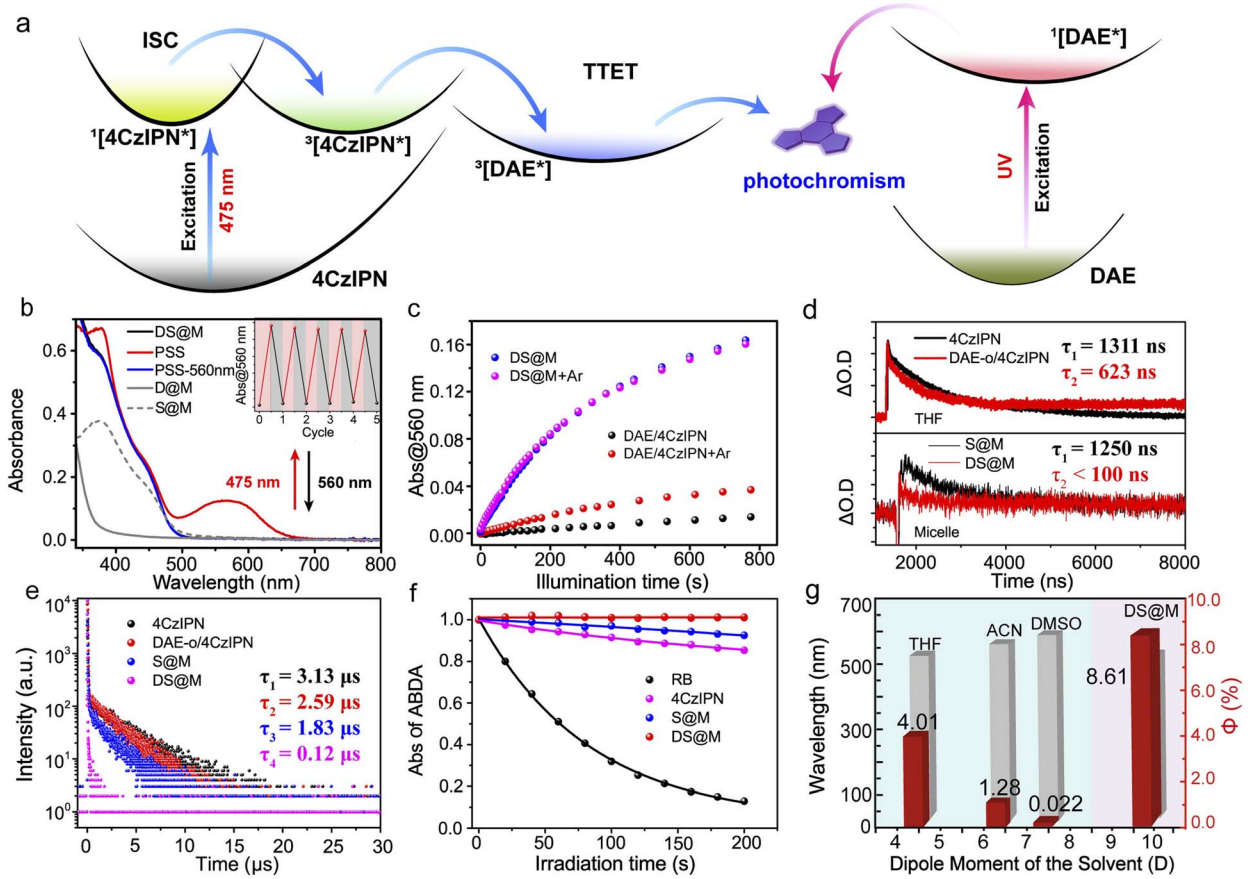

Fig. 2 (a) Illustration of the working mechanisms for TTET induced visible light photochromism with a narrow ΔE_{ST} sensitizer (left) and for photochromism of direct excitation (right). (b) The absorption of both **DAE** (grey) and **4CzIPN** sensitizer (grey dash) in micelles (**D@M** and **S@M**), respectively. The photochromic performance of **DS@M** in PBS buffer solution (2.5×10^{-5} M, 2 mL) under alternate 475/560 nm irradiation. **DS@M** before (black) and after 475 nm irradiation (red, PSS), and photo-decoloration upon 560 nm irradiation (blue). Inset: repetitive switching cycles of **DS@M** in PBS buffer solution (2.5×10^{-5} M, 2 mL) *via* alternate 475/560 nm irradiation. (c) Photocyclization performances of **DS@M** (2.5×10^{-5} M, 2 mL) in de-aerated (argon bubbled) PBS buffer (magenta), PBS buffer without argon bubbling (blue); **DAE/4CzIPN** (2.5×10^{-5} M, 2 mL) in de-aerated (argon bubbled) THF solution (red) and without argon bubbling (black). (d) Transient absorption decays of **4CzIPN** (1.0×10^{-4} M in 3 mL THF, top, black line), **DAE-o/4CzIPN** (1.0×10^{-4} M in 3 mL THF, top, red line), **S@M** (1.0×10^{-4} M in 3 mL PBS buffer, bottom, black line) and **DS@M** (1.0×10^{-4} M in 3 mL PBS buffer, bottom, red line) at 477 nm (LP-980 laser flash photolysis spectrometer setup). (e) The delayed luminescence lifetime spectra of **4CzIPN** (1.0×10^{-4} M in 3 mL THF, black), **DAE-o/4CzIPN** (1.0×10^{-4} M in 3 mL THF, red), **S@M** (1.0×10^{-4} M in 3 mL PBS buffer, blue) and **DS@M** (1.0×10^{-4} M in 3 mL PBS buffer, magenta) at 540 nm (FLS 1000 spectrofluorometer). (f) **ABDA** (9,10-anthracenediyl-bis (methylene)dimalonic acid) absorption at 398 nm as a function of time, induced by ROS generated from **RB** (Rose Bengal, black), **4CzIPN** (magenta), **S@M** (blue) and **DS@M** (red) upon white light irradiation. (g) Solvent-dependent photochromic performance of **DAE/4CzIPN** (red column) and the emission wavelength of **DAE/4CzIPN** in different de-aerated solvents (THF: tetrahydrofuran; ACN: acetonitrile; DMSO: dimethylsulfoxide; **DS@M**: in PBS buffer) (λ_{ex} = 365 nm, gray column), 2.5×10^{-5} M, 2 mL.

on triplet-sensitized visible-light photochromism of **DAE-o/4CzIPN** is apparent in bulk solution. The absorption band at 560 nm can be hardly observed upon 475 nm irradiation without de-aeration of the solution by argon bubbling (ΔA@560 nm = 0.015 for PSS; Φ_{o-c} = 0.89%; Fig. 2c and Table 1) as described before. Upon argon bubbling, moderate triplet-sensitized photochromism was detected (ΔA@560 nm = 0.038 for PSS; Φ_{o-c} = 4.01%; Fig. 2c and Table 1).

In contrast, micellar-confined **DS@M** exhibited identical triplet-sensitized photochromism with a steady fast photo-responsive rate (ΔA@560 nm = 0.16; Φ_{o-c} = 7.75% and 8.61%; Fig. 2c and Table 1) either following de-aeration or under ambient conditions. Even under oxygen bubbling, **DS@M** still maintained similar triplet-sensitized photochromism (ΔA@560 nm = 0.16; Φ_{o-c} = 7.61%; Fig. S11 and Table S1†). Moreover, the long-time persistence of oxygen-shielding of micelles was also tested and visible-light photochromism was kept almost unchanged in **DS@M** stored in the dark for 4 weeks (Fig. S3c†). All the above results demonstrated that the self-assembled amphiphilic layer affords good protection against oxygen quenching. Similar results could be drawn from the transient absorption spectroscopy and ROS (reactive oxygen species) generation measurements. Indeed, the triplet state lifetimes of **4CzIPN** in both **DS@M** and control **S@M** exhibited negligible difference before and after argon bubbling (Fig. S9† and Table 2). Nonetheless, a *ca.* 40%

Table 1 Photochromic quantum yields of **DS@M**[a] and **DAE/4CzIPN**[b] at different wavelengths[c]

Photoreaction	λ (nm)	Φ (%)
DAE-o → **DAE-c** (with **4CzIPN** in THF)	475	0.89
DAE-o → **DAE-c** (with **4CzIPN** in **DS@M**)	475	7.75
DAE-o → **DAE-c** (with **4CzIPN** in THF, argon bubbling)	475	4.01
DAE-o → **DAE-c** (with **4CzIPN** in **DS@M**, argon bubbling)	475	8.61
DAE-c → **DAE-o** (with **4CzIPN** in THF)	560	0.42
DAE-c → **DAE-o** (with **4CzIPN** in **DS@M**)	560	0.13
DAE-o → **DAE-c** (with **4CzIPN** in **DS@M**)	313	7.80

[a] [**DS@M**] = 2.5×10^{-5} M. [b] [**DAE**] = [**4CzIPN**] = 2.5×10^{-5} M. [c] At 300 K.

decrease in the triplet state lifetime of **4CzIPN** in the bulk solution of **DAE-o**/**4CzIPN** was obtained (Fig. S9† and Table 2). In ROS generation measurement, the ROS yield of 4CzIPN in the bulk solution is 15.61%, while that of **DS@M** is 0.34% (Fig. 2f), confirming again the oxygen-shielding effect of micelle nanoconfinement.

Besides the oxygen quenching, solvent polarity is another factor that affects the efficiency of triplet sensitization.[20,45] The polarity-dependence of triplet-sensitized visible-light photochromism originates from the donor–acceptor structure of the narrow ΔE_{ST} sensitizer, for which the solvent polarity modulates the excited-state energy levels as well as the triplet-energy transfer process.[54] As the solvent polarity increases, the emission of **4CzIPN** undergoes an obvious red-shift from 514 nm in toluene to 566 nm in dimethylsulfoxide (Fig. 2g, blue region; Fig. S12†), implying a stabilization of the excited-state energy level of the sensitizer. Correspondingly, the photoswitching quantum yield upon 475 nm irradiation varies slightly in de-aerated apolar solvents (Φ_{o-c} = 5.26% in toluene and Φ_{o-c} = 4.01% in THF), while it shows an abrupt decrease in de-aerated highly polar acetonitrile (Φ_{o-c} = 1.28%) and is almost negligible in dimethylsulfoxide (Φ_{o-c} = 0.022%; Fig. 2g, blue region; Fig. S12†). This effect is likely due to the mismatch between the energetically perturbed triplet state of the **4CzIPN** sensitizer and that of the **DAE-o** photoswitch in polar solvents. Delightfully, in the **DS@M** nanoconfinement, the **mPEG-DSPE** shell successfully isolates the incorporated **DAE-o**/**4CzIPN** pair from the interference of external polarity and maintains an appropriate environment (polarity close to THF according to the emission spectra) for efficient visible-light photoswitching to proceed, even in PBS buffer (de-aerated; Fig. 2g, pink region). Thus, the micelle nanoconfinement acts as a dual shield (from both oxygen and solvent polarity) to provide an optimal environment for triplet-sensitized photochromism.

Amplified fluorescence switching for high-contrast ON/OFF modulation

Given the fast and efficient photochromism in **DS@M** micelles, we then investigated the photo-induced fluorescence signal modulation within the nanoconfinement. Taking advantage of the emissive properties of **4CzIPN** and the spectral overlap between **4CzIPN** emission and **DAE-c** absorption (Fig. 3b), **4CzIPN** may act not only as a triplet-sensitizer but also as a FRET donor. Theoretical calculations were carried out at the B3LYP/6-31 G(d) level of theory. The band gap of **4CzIPN** is obviously lower than that of **DAE-o**, but close to that of **DAE-c**, indicating a good spectral overlap between the two (Fig. 3a and Table S3†). Since the FRET efficiency is inversely proportional to the sixth power of donor–acceptor distance, the micelle nanoconfinement is expected to promote FRET between **DAE-c** and **4CzIPN** compared to that in bulk solution. As shown in Fig. 3c, 475 nm irradiation led to a nearly quantitative quenching of **DS@M** fluorescence at 540 nm, while the fluorescence of **DAE**/**4CzIPN** dispersed in THF exhibited only a modest quenching of merely 50% and 25% upon the exposure to UV (365 nm) and visible light (475 nm), respectively (Fig. S13†). More importantly, a fast decline of emission intensity took place as the fluorescence of **4CzIPN** was quenched dramatically at the initial stage (Fig. 3d). About 50% of fluorescence emission is quenched with only *ca.* 0.6% photoswitching ratio (<1 s), and quenched to 10% with a photo-conversion ratio of 10%. The intensity could finally decrease to a residue of <7% when PSS is reached. The FRET efficiency was calculated as ET = 94.5% with an R_{DA} = 1.22 nm through a theoretical model (Table S4; see the ESI† for details), which is comparable to the experimental outcomes.

Fluorescence lifetime studies were conducted to investigate the FRET process in micelles. An evident variation was observed through photo-switching in **DS@M** (τ_{on} = 13.17 ns to τ_{off} = 4.13 ns; Fig. S14† and Table 2). In comparison, a slight fluorescence

Table 2 Triplet state and fluorescence/phosphorescence lifetimes of **S@M**, **DS@M** in PBS buffer and **4CzIPN**, **DAE/4CzIPN** in THF

Lifetimes	S@M	DS@M	4CzIPN	DAE/4CzIPN
Triplet state (without argon)	1238 ns	<100 ns	504 ns	446 ns
Triplet state (with argon)	1250 ns	<100 ns	1311 ns	623 ns
Prompt fluorescence	13.17 ns	4.13 ns (in PSS)	18.13 ns	17.52 ns (in PSS)
Delayed fluorescence	1.83 μs	0.12 μs	3.13 μs	2.59 μs
Phosphorescence	1368 μs	780 μs	1757 μs	1679 μs

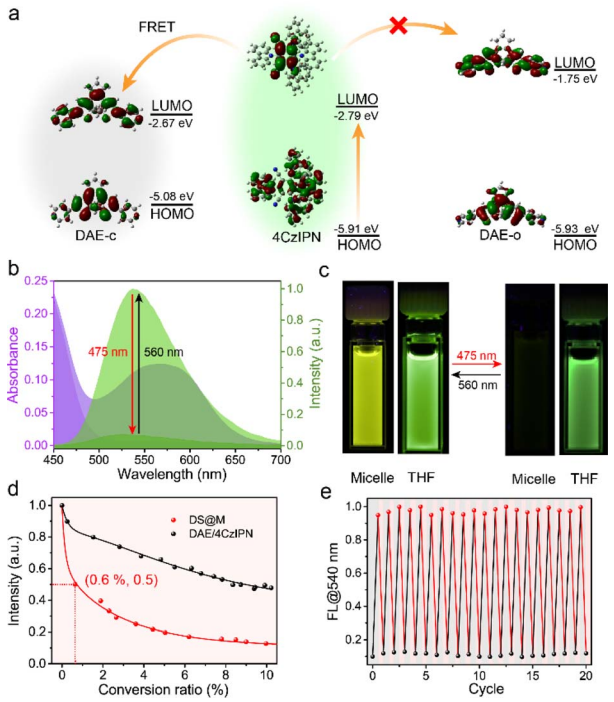

Fig. 3 (a) The working mechanism for the FRET between **4CzIPN** and **DAE-c**. (b) Absorption and normalized emission spectra of **DS@M** in PBS buffer solution (2.5×10^{-5} M, 2 mL) in its open-form (absorption: dark violet shadow, fluorescence: light green shadow) and PSS state (absorption: light violet shadow, fluorescence: dark green shadow). (c) Photographs of fluorescence changes of **DS@M** in PBS buffer and **DAE/4CzIPN** in THF before and after irradiation. (d) Fluorescence intensity *versus* conversion ratio correlation plots: **DS@M** (red) in PBS buffer solution (2.5×10^{-5} M, 2 mL) under 475 nm light and **DAE/4CzIPN** (black) in THF solution (2.5×10^{-5} M, 2 mL) under UV light. (e) Normalized emission spectra of **DS@M** in PBS buffer solution (2.5×10^{-5} M, 2 mL) were recorded for 20 cycles of 475 nm/560 nm irradiation.

lifetime change was detected before and after photoisomerization ($\tau_{on} = 18.13$ ns to $\tau_{off} = 17.52$ ns; Fig. S14† and Table 2) of **DAE/4CzIPN** in bulk solution, which is in accordance with the low quenching ratio as well as the inefficient triplet-sensitized photochromism. The fluorescence energy transfer rate constant in the **DS@M** nanoconfinement was determined as $k_{ET} = 6.86 \times 10^{13}$ s^{-1} *via* the Stern–Volmer equation (Fig. S15 and Table S4; see the ESI† for details), much larger than the diffusion rate constant in solution ($\sim 10^{10}$ s^{-1}). Therefore, the limited diffusion and shortened donor–acceptor distance within the micelles facilitates amplified fluorescence on/off switching,[55] ensuring a fast and high-contrast signal photomodulation in **DS@M**. The emission was restored to its original intensity after irradiation with 560 nm light and the fluorescence on/off modulation lasted more than 20 cycles with negligible degradation (Fig. 3e and S16†). The fast responsiveness and high-contrast fluorescence on/off modulation, together with the robust fatigue resistance of **DS@M**, render a short operation/exposure time as well as high-resolution signal acquisition, which are critical for its successful deployment in the following applications.

Instant photo-patterning for information encryption

We initially sought to exploit the potential application of the **DS@M** nanoconfinement system as information storage medium in the aqueous phase, by taking full advantage of its enhanced photoswitching efficiency and fast responsiveness. **DS@M** was introduced into a hydrogel network by immersing the hyaluronic acid gel in micellar solution (Fig. 4a). The prepared hydrogel showed bright yellow-green fluorescence attributed to the encapsulated **4CzIPN** in the micelles. An instant patterning of a fluorescent QR code on the gel was achieved upon a 475 nm light flash (10 mW cm^{-2}, <1 s) through a customized mask. As a result of the fast and high-contrast fluorescence photo-modulation, the encoded image exhibited high resolution in a quasi-liquid hydrogel, which could be easily decoded by a smartphone (Fig. 4b). It should be emphasized that the "amplified fluorescence modulation" requires only minute coloration of photochromic dyes,[55] resulting in a hardly discernible color change in the fluorescently encoded QR code hydrogel (Fig. S17†). In addition, we also demonstrated the immediate inscription of information on the hydrogel at the speed of normal handwriting using a hand-held 450 nm laser pointer (5 W, Video S1†), by virtue of the rapid light-induced quenching of **DS@M** micelle systems (Fig. S18†). All encoded patterns and inscriptions can be erased by illumination at 560 nm, permitting erasable and recyclable information storage, suggesting further applications of this photoswitchable fluorescent hydrogel medium in encrypted information storage and anti-counterfeiting technologies.[56]

Photoswitchable fluorescence for dynamic intracellular imaging

Encouraged by the bio-compatible visible-light photochromism of the **DS@M** system as well as the high-contrast, robust photo-induced fluorescence on–off modulation (both intensity and lifetime), we further evaluated the applicability of our **DS@M** nanoconfinement for multi-model intracellular imaging. To explore the bioimaging performance of our micellar system, we first incubated HeLa (human cervical cancer) cells with **DS@M**

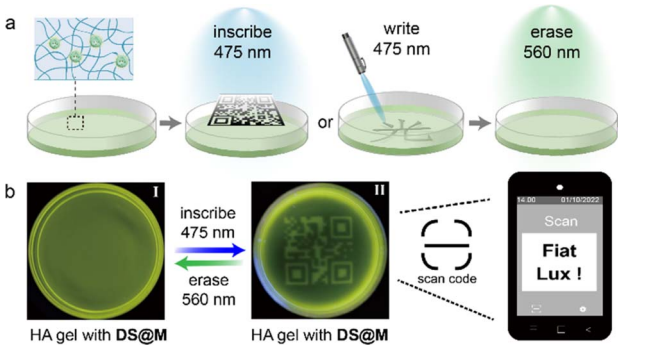

Fig. 4 (a) Schematic representation of instant photo-patterning for information encryption. (b) The fluorescent readable QR-code was inscribed onto and erased from the **DS@M** dispersed hydrogel using 475 nm and 560 nm light, which could be decoded using a smartphone.

micellar solution (10 μM) for 30 min. The cells exhibited yellow-green fluorescence under confocal imaging, indicating that the micelles were successfully internalized into HeLa cells (Fig. S19†). Since micelle nanoparticles are prone to be trafficked to the lysosome,[57] co-localization of **DS@M** in both lysosome and mitochondria was carried out. Co-localization of **DS@M** fluorescence with that of a lyso-tracker (Lyso-Tracker Red) and a mito-tracker (Mito-Tracker Deep Red 633) showed that the micelles were largely assembled in the lysosome (Pearson's correlation coefficient of 0.87, Fig. S20†) rather than in mitochondria (Pearson's correlation coefficient of 0.59, Fig. S21†). Meanwhile, the colorimetric CCK-8 assay demonstrated only little cytotoxicity of micelles (Fig. S22†), thus suggesting the good bio-compatibility of **DS@M** for bioimaging applications.

Subsequently, 475/560 nm light irradiation of the HeLa cells was performed, and a reversible off–on alternation of fluorescence signal was acquired (Fig. 5a and S23†). Upon 475 nm irradiation (10 mW cm^{-2}), the intracellular fluorescence is almost completely quenched. In contrast, the subsequent 560 nm irradiation (30 mW cm^{-2}) recovered fluorescence to the initial state (Fig. S23 and S24†). Remarkably, this photo-blinking effect was repeated over several cycles with no obvious fluorescence attenuation (Fig. 5a(III)). In addition to fluorescence intensity, the photo-switchable signal was also visualized through fluorescence lifetime imaging microscopy (FLIM). Upon alternate 475/560 nm irradiation, switchable lifetimes (τ_{on} = 12.97 ns ↔ τ_{off} = 4.76 ns) *via* effective FRET can be observed (Fig. S25†). As a result, fluorescence lifetime,[58] an inherent photophysical property of chromophores, can be combined with intensity as another mode of signal to achieve photo-reversible confocal and time-resolved fluorescence bio-imaging. This dynamic, all-visible-light switchable signal offers an alternative "double-check" strategy to differentiate from auto-biofluorescence and enhance the imaging precision: (1) the cycling "on–off–on" fluorescence intensity gives a higher authenticity towards traditional one-time "on–off" or "off–on" probing.[59,60] (2) The cycling feature of the lifetime amplifies the signal-to-noise ratio even with short lifetime fluorophores (12.97 ns in this work, Fig. 5b(III)), compared with the traditional lifetime methods in which long lifetime probes (μs–ms) are necessary to minimize the auto-biofluorescence disturbance.[61]

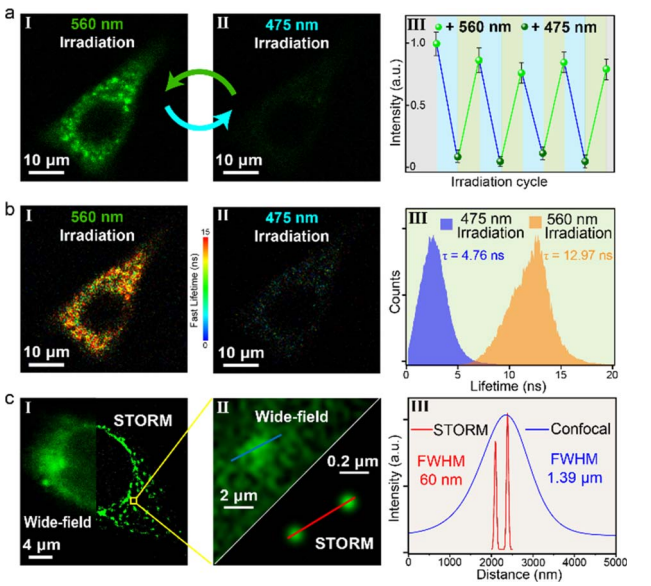

Fig. 5 (a) Fluorescence confocal imaging (I and II, scale bar: 10 μm) and intracellular fluorescence intensity switching (III) of HeLa cells incubated with DS@M (10 μM), upon alternate irradiation with 475/560 nm light (excitation: 475 nm; emission: 500–650 nm; irradiation with 475 nm: 10 mW cm^2; irradiation with 560 nm: 30 mW cm^{-2}). (b) Fluorescence lifetime imaging (I and II, scale bar: 10 μm) and FLIM histogram (III) of HeLa cells incubated with DS@M (10 μM), upon alternate irradiation with 475/560 nm light. Scale bar: 10 μm; color bar: fast lifetimes (ns). (c) Super-resolution STORM (right) and conventional wide-field (left) images of the HeLa cell (I, scale bar: 4 μm). Calculation of FWHM in HeLa cells of the STORM image and wide-field image, respectively (II and III).

Diarylethene is regarded as one of the most promising synthetic photoswitches that modulate fluorescence for super-resolution imaging.[62–65] Next, a super-resolution microscopy image of a single HeLa cell with **DS@M** was achieved under the STORM setup.[65–67] Micelles were found to enter cells by nonspecific endocytosis and were uniformly distributed in cells (Fig. 5c). In the wide-field region, individual micelles cannot be distinguished due to the close inter-micelle distance and the resolution of the corresponding position (FWHM, full width at half-maximum) is 1.39 μm (Fig. 5c(III) and S26†). Switching between the on/off states of **DS@M** was performed by laser irradiation with 561 nm and 488 nm light, respectively. The measurement was initialized by 488 nm illumination to switch all micelles in the observation area to the "dark" state. Under 561 nm laser, a tiny amount of micelles was activated and then excited with a 488 nm laser to emit fluorescence. STORM images were recorded on an electron-multiplying charge-coupled device (EMCCD) camera running at 20 ms per frame. After the optimization of the protocol (see the ESI† for details),[67] super-resolution images were reconstructed from the up to 10000 frames, using the N-STORM analysis module of NIS Elements AR (Laboratory Imaging s.r.o.), and the fluorescence signal of the image was processed with the Image J software. To our delight, STORM images displayed clear nano-sized localizations of separated micelles. Fig. 5c shows the FWHM value of the localized fluorescence points, which can be determined by Gaussian fitting to be as narrow as 60 nm, well beyond the diffraction limit of light. Moreover, Fourier ring correlation (FRC) was utilized to calculate the resolution as 51 nm (Fig. S27†), in good agreement with the FWHM value derived from Gaussian fitting. It should be noted that the values obtained above are comparable with the hydrodynamic size of **DS@M** and that an over 20-fold enhanced resolution than that obtained through conventional wide-field imaging is successfully achieved, hence corroborating the potential capability of our visible-light responsive nanoconfinement system for biocompatible nanoimaging.

Conclusions

In this work, we fabricated an optically controllable nanoconfined system based on a combination of three components –

a diarylethene photoswitch (**DAE**), a triplet-sensitizer (**4CzIPN**) and an amphiphile (**mPEG-DSPE**) – that formed a visible-light switchable micelle, **DS@M**. The encapsulation of **DAE**/**4CzIPN** pairs inside the small-sized micelle (~40 nm) enables a distinct nanoconfinement effect that eliminates both distance-dependence and environmental sensitivity (shielding the system from oxygen quenching and solvent polarity) of the Dexter-type triplet-sensitization process. A remarkable 9-fold enhancement of the triplet–triplet energy transfer (TTET) induced visible-light photochromism and a consequential accelerated/high-contrast fluorescence modulation ($k_{ET} = 6.86 \times 10^{13}$ s^{-1}, ET = 94.5%) were exhibited in **DS@M** compared to when the components were present at equivalent concentrations in freely diffusional bulk solutions. Based on its excellent light-switchable performance, the proof-of-concept applications of instant photo-patterning/encryption in **DS@M** containing hydrogels and all-visible-light (488/561 nm) operated confocal and super-resolution imaging of HeLa cells were successfully realized. We anticipate that this new strategy towards optimizing the performance and biocompatibility of triplet-sensitized visible-light photoswitches will pave the way to the construction of further visible-light responsive nano-systems ideally suited to fulfill versatile applications in materials and life science.

Data availability

All experimental data and detailed experimental procedures are available in the main text and ESI.†

Author contributions

W. W. and W. Y. synthesized all the materials, performed all photophysical property measurements in solution and analyses, and prepared the paper. Z. Z. assisted in the synthesis of some intermediate products and the instant patterning application. J. D. incubated HeLa cells and conducted the imaging test. Y. X. helped in the preparation of micelles. J. Z. designed and supervised the research and wrote the paper. All authors discussed the results and commented on the manuscript.

Conflicts of interest

There are no conflicts to declare.

Acknowledgements

This work was supported by NSFC (22122803, 22101084, 22378121), Shanghai Municipal Science and Technology Major Project (2018SHZDZX03), the international cooperation program of Shanghai Science and Technology Committee (17520750100), and the Fundamental Research Funds for the Central Universities (222201717003). JZ acknowledges Shanghai Natural Science Foundation Project (23ZR1479500). The authors wish to acknowledge Zhiyuan Zeng and Jingran Liu for help in micelle preparation.

Notes and references

1 J. Volaric, W. Szymanski, N. A. Simeth and B. L. Feringa, *Chem. Soc. Rev.*, 2021, **50**, 12377–12449.
2 M. Irie, T. Fukaminato, K. Matsuda and S. Kobatake, *Chem. Rev.*, 2014, **114**, 12174–12277.
3 Z. Zhang, W. Wang, M. O'Hagan, J. Dai, J. Zhang and H. Tian, *Angew. Chem., Int. Ed.*, 2022, **61**, e202205758.
4 D. Bleger and S. Hecht, *Angew. Chem., Int. Ed.*, 2015, **54**, 11338–11349.
5 S. He, J. Song, J. Qu and Z. Cheng, *Chem. Soc. Rev.*, 2018, **47**, 4258–4278.
6 S. Wang, B. Li and F. Zhang, *ACS Cent. Sci.*, 2020, **6**, 1302–1316.
7 R. Weinstain, T. Slanina, D. Kand and P. Klán, *Chem. Rev.*, 2020, **120**, 13135–13272.
8 N. M. Wu, M. Ng, W. H. Lam, H. L. Wong and V. W. Yam, *J. Am. Chem. Soc.*, 2017, **139**, 15142–15150.
9 T. Fukaminato, T. Hirose, T. Doi, M. Hazama, K. Matsuda and M. Irie, *J. Am. Chem. Soc.*, 2014, **136**, 17145–17154.
10 Z. Li, Y. Dai, Z. Lu, Y. Pei, H. Chen, L. Zhang, Y. Duan and H. Guo, *Chem. Commun.*, 2019, **55**, 13430–13433.
11 G. Liu, Y. M. Zhang, C. Wang and Y. Liu, *Chem.–Eur. J.*, 2017, **23**, 14425–14429.
12 A. Kometani, Y. Inagaki, K. Mutoh and J. Abe, *J. Am. Chem. Soc.*, 2020, **142**, 7995–8005.
13 M. M. Lerch, S. J. Wezenberg, W. Szymanski and B. L. Feringa, *J. Am. Chem. Soc.*, 2016, **138**, 6344–6347.
14 K. Klaue, Y. Garmshausen and S. Hecht, *Angew. Chem., Int. Ed.*, 2018, **57**, 1414–1417.
15 J. Gemen, J. R. Church, T. P. Ruoko, N. Durandin, M. J. Bialek, M. Weissenfels, M. Feller, M. Kazes, M. Odaybat, V. A. Borin, R. Kalepu, Y. Diskin-Posner, D. Oron, M. J. Fuchter, A. Priimagi, I. Schapiro and R. Klajn, *Science*, 2023, **381**, 1357–1363.
16 M. Herder, B. M. Schmidt, L. Grubert, M. Patzel, J. Schwarz and S. Hecht, *J. Am. Chem. Soc.*, 2015, **137**, 2738–2747.
17 S. Fredrich, R. Gostl, M. Herder, L. Grubert and S. Hecht, *Angew. Chem., Int. Ed.*, 2016, **55**, 1208–1212.
18 J. Isokuortti, K. Kuntze, M. Virkki, Z. Ahmed, E. Vuorimaa-Laukkanen, M. A. Filatov, A. Turshatov, T. Laaksonen, A. Priimagi and N. A. Durandin, *Chem. Sci.*, 2021, **12**, 7504–7509.
19 Z. Zhang, J. Zhang, B. Wu, X. Li, Y. Chen, J. Huang, L. Zhu and H. Tian, *Adv. Opt. Mater.*, 2018, **6**, 1700847.
20 Z. Zhang, W. Wang, P. Jin, J. Xue, L. Sun, J. Huang, J. Zhang and H. Tian, *Nat. Commun.*, 2019, **10**, 4232.
21 W. Danowski, F. Castiglioni, A. S. Sardjan, S. Krause, L. Pfeifer, D. Roke, A. Comotti, W. R. Browne and B. L. Feringa, *J. Am. Chem. Soc.*, 2020, **142**, 9048–9056.
22 M. Liu, P. Xia, G. Zhao, C. Nie, K. Gao, S. He, L. Wang and K. Wu, *Angew. Chem., Int. Ed.*, 2022, **61**, e202208241.
23 V. W.-W. Yam, C.-C. Ko and N. Zhu, *J. Am. Chem. Soc.*, 2004, **126**, 12734–12735.

24 M. T. Indelli, S. Carli, M. Ghirotti, C. Chiorboli, M. Ravaglia, M. Garavelli and F. Scandola, *J. Am. Chem. Soc.*, 2008, **130**, 7286–7299.
25 L. Hou, W. Larsson, S. Hecht, J. Andréasson and B. Albinsson, *J. Mater. Chem. C*, 2022, **10**, 15833–15842.
26 W. Larsson, M. Morimoto, M. Irie, J. Andreasson and B. Albinsson, *Chem.–Eur. J.*, 2023, **29**, e202203651.
27 A. Tokunaga, L. M. Uriarte, K. Mutoh, E. Fron, J. Hofkens, M. Sliwa and J. Abe, *J. Am. Chem. Soc.*, 2019, **141**, 17744–17753.
28 L. Pfeifer, N. V. Hoang, M. Scherübl, M. S. Pshenichnikov and B. L. Feringa, *Sci. Adv.*, 2020, **6**, eabb6165.
29 K. Mori, Y. Ishibashi, H. Matsuda, S. Ito, Y. Nagasawa, H. Nakagawa, K. Uchida, S. Yokojima, S. Nakamura, M. Irie and H. Miyasaka, *J. Am. Chem. Soc.*, 2011, **133**, 2621–2625.
30 S. Dutta, J. R. Whicher, D. A. Hansen, W. A. Hale, J. A. Chemler, G. R. Congdon, A. R. H. Narayan, K. Håkansson, D. H. Sherman, J. L. Smith and G. Skiniotis, *Nature*, 2014, **510**, 512–517.
31 B. C. Tripp, K. Smith and J. G. Ferry, *J. Biol. Chem.*, 2001, **276**, 48615–48618.
32 A. Valentini, M. Nucci, L. M. Frutos and M. Marazzi, *ChemPhotoChem*, 2019, **3**, 925–932.
33 P. Duan, N. Yanai, H. Nagatomi and N. Kimizuka, *J. Am. Chem. Soc.*, 2015, **137**, 1887–1894.
34 J. S. Trimble, R. Crawshaw, F. J. Hardy, C. W. Levy, M. J. B. Brown, D. E. Fuerst, D. J. Heyes, R. Obexer and A. P. Green, *Nature*, 2022, **611**, 709–714.
35 N. Sun, J. Huang, J. Qian, T.-P. Zhou, J. Guo, L. Tang, W. Zhang, Y. Deng, W. Zhao, G. Wu, R.-Z. Liao, X. Chen, F. Zhong and Y. Wu, *Nature*, 2022, **611**, 715–720.
36 K. Liu, X. Qiao, C. Huang, X. Li, Z. Xue and T. Wang, *Angew. Chem., Int. Ed.*, 2021, **60**, 14365–14369.
37 G. Naren, C.-W. Hsu, S. Li, M. Morimoto, S. Tang, J. Hernando, G. Guirado, M. Irie, F. M. Raymo, H. Sundén and J. Andréasson, *Nat. Commun.*, 2019, **10**, 3996.
38 C. H. Foyer and G. Hanke, *Plant J.*, 2022, **111**, 642–661.
39 A. Pannwitz and O. S. Wenger, *Chem. Commun.*, 2019, **55**, 4004–4014.
40 J. C. Valmalette, A. Dombrovsky, P. Brat, C. Mertz, M. Capovilla and A. Robichon, *Sci. Rep.*, 2012, **2**, 579.
41 K. Kalyanasundaram, F. Grieser and J. K. Thomas, *Chem. Phys. Lett.*, 1975, **51**, 501–505.
42 F. Pina, A. J. Parola, E. Ferreira, M. Maestri, N. Armaroli, R. Ballardini and V. Balzani, *J. Phys. Chem.*, 1995, **99**, 12701–12703.
43 W. M. Nau and X. Zhang, *J. Am. Chem. Soc.*, 1999, **121**, 8022–8032.
44 S. A. Gerhardt, J. W. Lewis, D. S. Kliger, J. Z. Zhang and U. Simonis, *J. Phys. Chem. A*, 2003, **107**, 2763–2767.
45 P. Bharmoria, S. Ghasemi, F. Edhborg, R. Losantos, Z. Wang, A. Martensson, M. Morikawa, N. Kimizuka, U. Isci, F. Dumoulin, B. Albinsson and K. Moth-Poulsen, *Chem. Sci.*, 2022, **13**, 11904–11911.
46 D. Kim, K. Jeong, J. E. Kwon, H. Park, S. Lee, S. Kim and S. Y. Park, *Nat. Commun.*, 2019, **10**, 3089.
47 H. B. Cheng, B. Qiao, H. Li, J. Cao, Y. Luo, K. M. Kotraiah Swamy, J. Zhao, Z. Wang, J. Y. Lee, X. J. Liang and J. Yoon, *J. Am. Chem. Soc.*, 2021, **143**, 2413–2422.
48 J. Park, M. Xu, F. Li and H. C. Zhou, *J. Am. Chem. Soc.*, 2018, **140**, 5493–5499.
49 M. P. O'Hagan, S. Haldar, M. Duchi, T. A. A. Oliver, A. J. Mulholland, J. C. Morales and M. C. Galan, *Angew. Chem., Int. Ed.*, 2019, **58**, 4334–4338.
50 L. Pesce, C. Perego, A. B. Grommet, R. Klajn and G. M. Pavan, *J. Am. Chem. Soc.*, 2020, **142**, 9792–9802.
51 D. Samanta, D. Galaktionova, J. Gemen, L. J. W. Shimon, Y. Diskin-Posner, L. Avram, P. Kral and R. Klajn, *Nat. Commun.*, 2018, **9**, 641.
52 M. Canton, A. B. Grommet, L. Pesce, J. Gemen, S. Li, Y. Diskin-Posner, A. Credi, G. M. Pavan, J. Andreasson and R. Klajn, *J. Am. Chem. Soc.*, 2020, **142**, 14557–14565.
53 W. S. Saad and R. K. Prud'homme, *Nano Today*, 2016, **11**, 212–227.
54 M. Wang, T. Chatterjee, C. J. Foster, T. Wu, C.-L. Yi, H. Yu, K.-T. Wong and B. Hu, *J. Mater. Chem. C*, 2020, **8**, 3395–3401.
55 J. Su, T. Fukaminato, J. P. Placial, T. Onodera, R. Suzuki, H. Oikawa, A. Brosseau, F. Brisset, R. Pansu, K. Nakatani and R. Metivier, *Angew. Chem., Int. Ed.*, 2016, **55**, 3662–3666.
56 Z. Li, X. Liu, G. Wang, B. Li, H. Chen, H. Li and Y. Zhao, *Nat. Commun.*, 2021, **12**, 1363.
57 C. Yu, B. He, M. H. Xiong, H. Zhang, L. Yuan, L. Ma, W. B. Dai, J. Wang, X. L. Wang, X. Q. Wang and Q. Zhang, *Biomaterials*, 2013, **34**, 6284–6298.
58 M. Yu, W. Zhao, F. Ni, Q. Zhao and C. Yang, *Adv. Opt. Mater.*, 2022, **10**, 2102437.
59 J. Zhang, Y. Fu, H. H. Han, Y. Zang, J. Li, X. P. He, B. L. Feringa and H. Tian, *Nat. Commun.*, 2017, **8**, 987.
60 Y. Fu, H. H. Han, J. Zhang, X. P. He, B. L. Feringa and H. Tian, *J. Am. Chem. Soc.*, 2018, **140**, 8671–8674.
61 Y. Xie, M. C. Arno, J. T. Husband, M. Torrent-Sucarrat and R. K. O'Reilly, *Nat. Commun.*, 2020, **11**, 2460.
62 B. Roubinet, M. Weber, H. Shojaei, M. Bates, M. L. Bossi, V. N. Belov, M. Irie and S. W. Hell, *J. Am. Chem. Soc.*, 2017, **139**, 6611–6620.
63 B. Roubinet, M. L. Bossi, P. Alt, M. Leutenegger, H. Shojaei, S. Schnorrenberg, S. Nizamov, M. Irie, V. N. Belov and S. W. Hell, *Angew. Chem., Int. Ed.*, 2016, **55**, 15429–15433.
64 D. Kim, A. Aktalay, N. Jensen, K. Uno, M. L. Bossi, V. N. Belov and S. W. Hell, *J. Am. Chem. Soc.*, 2022, **144**, 14235–14247.
65 H. Yang, M. Li, C. Li, Q. Luo, M. Q. Zhu, H. Tian and W. H. Zhu, *Angew. Chem., Int. Ed.*, 2020, **59**, 8560–8570.
66 Z. Ye, H. Yu, W. Yang, Y. Zheng, N. Li, H. Bian, Z. Wang, Q. Liu, Y. Song, M. Zhang and Y. Xiao, *J. Am. Chem. Soc.*, 2019, **141**, 6527–6536.
67 X. Chai, H. H. Han, A. C. Sedgwick, N. Li, Y. Zang, T. D. James, J. Zhang, X. L. Hu, Y. Yu, Y. Li, Y. Wang, J. Li, X. P. He and H. Tian, *J. Am. Chem. Soc.*, 2020, **142**, 18005–18013.